PSFC/JA-12-7

Test of a conduction-cooled, prototype, superconducting magnet for a compact cyclotron

P.C. Michael

March 2012

Plasma Science and Fusion Center
Massachusetts Institute of Technology
Cambridge MA 02139 USA

This work was supported in part by a Frontiers in Science grant of the Defense Threat Reduction Agency HDTRA-09-1-00042, and by Pennsylvania State University, Advanced Research Laboratory Sub-contract SL11-06: Superconducting cyclotron with integral secondary beam production target.

Summary: A small, conduction-cooled Nb_3Sn superconducting coil in iron yoke was tested to failure during the week of Jan. 30, 2012. The tests were performed to examine cooling and assembly techniques relevant to the Nanotron program.

This memo summarizes the thermal, electrical and electromagnetic data collected during the tests. The heat loads on the coil system were dominated by thermal conduction along and resistive dissipation in the coil current leads. The results indicate that it is technically feasible to design the Nanotron coil to operate at currents above 200 A.

Test arrangement: Fig. 1 shows a schematic cross section of the conduction-cooled Nanotron prototype magnet suspended within its 0.76 m diameter, 1 m tall vacuum chamber. Table 1 summarizes dimensions for the Nb_3Sn coil and surrounding iron yoke.

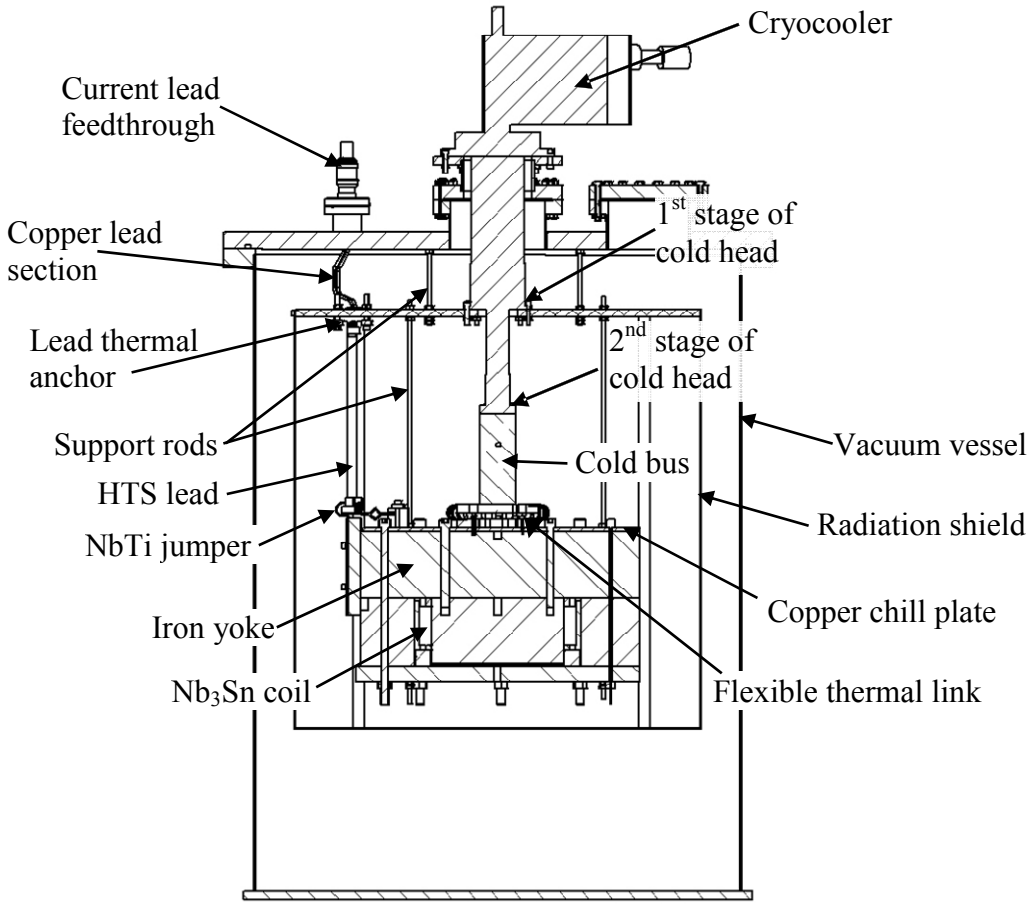

Fig. 1: Cross-sectional view of the test apparatus.

Table 1: Magnet parameters

Conductor type	Internal-tin strand
Conductor diameter	0.813 mm
Conductor copper to non-copper ratio	1.38:1
Conductor insulation	S-2 glass
Diameter over conductor insulation	0.962 mm
Inner diameter of Nb_3Sn winding	208.5 mm
Outer diameter of Nb_3Sn winding	245.7 mm
Height of Nb_3Sn winding	61.6 mm
Number of layers in winding	22
Numbers of turns per layer	63
Iron yoke material	A36 steel
Outer diameter of iron yoke	444.5 mm
Height of iron yoke	237.5 mm
Mass of iron yoke	270 kg

The Nb_3Sn winding was fabricated by Superconducting Systems, Inc. of Billerica, MA using internal-tin type Nb_3Sn strand remaining from the ITER CS model coil program. After its reaction heat treatment the winding was encased in an aluminum housing and vacuum pressure impregnated using CTD 512 epoxy. During processing, three ~30 mm lengths of 0.75 mm diameter NbTi-type superconductor were soldered to each coil terminal to facilitate subsequent attachment to the test apparatus' current leads. Details of the coil fabrication can be found in [1].

The prototype winding and iron yoke are together suspended by three 586.6 mm long ¼-20 threaded stainless-steel rods, attached to the 12.7 mm thick, 638 mm diameter top plate of the copper radiation shield that completely surrounds the magnet assembly. The outer surface of the iron yoke was covered with 3M series 425 aluminum tape to minimize radiant heat transfer from the radiation shield to the magnet [2]. The top plate of the radiation shield is similarly suspended by three 106 mm long ¼-20 stainless steel rods attached to the underside of the vacuum vessel cover plate. The 660 mm tall radiation shield can was completely surrounded by 25 layers of 6.4 μm thick, double-aluminized polyester film procured from Rol-Vac LP of Dayville, CT. The layers are not shown in Fig. 1. Considerable care was taken not to wrap too tightly and to interleave the ends and sides of this multi-layer insulation (MLI) layer to minimize radiant heat transfer from the vacuum vessel walls to the shield.

Conduction cooling for the test assembly is provided by a Leybold RDK-408D2 cryocooler. This cryocooler was reconditioned and its performance was recharacterized in our laboratory during Nov. 2011 before being integrated with the test apparatus. The first stage of the cryocooler cold head is rigidly attached to the radiation shield plate, whereas the second stage of the cold head is attached to the magnet through a flexible thermal link. This arrangement ensures the highest possible heat removal rate at the first stage of the cold head, where both temperatures and heat loads are greater, while still permitting relative differential thermal contraction between components as the apparatus cools from room temperature. A 55.9 mm diameter, 143.5 mm long, high-conductivity copper cold bus was inserted between the 2nd stage of the cold head and this flexible link to permit the approximately 300 mm long HTS leads to be installed vertically. The 6.3 mm thick copper chill plate affixed to the upper surface of the yoke provides the magnet assembly with a reasonably uniform thermal operating environment. This chill plate also

provides a low thermal resistance path to remove the heat conducted through the HTS current leads to the magnet assembly.

The coil terminals are connected to an external power supply through a pair of multi-stage current leads. Current enters the vacuum chamber through a pair of high-current feedthroughs. Each feedthrough contains a 19 mm diameter solid copper electrode that is sealed partway along its length to an electrical insulator, which in turn is sealed to a vacuum flange that bolts to the test chamber cover plate. The electrode protrudes about 108.5 mm into the vacuum space. The remaining portion of the copper section of the current lead was inadvertently optimized, according to the design rules proposed by McFee [3], for operation at 600 A.

Fig. 2a shows the arrangement of the copper portion of the current leads. The final 25 mm length of the in-vacuum end of the feedthrough electrode was sectioned to provide a split clamp into which two 157.5 mm lengths of 4.62 mm diameter (6 AWG) copper magnet wire were inserted. The intended 350 A optimized current lead would have used a slightly smaller (3.26 mm diameter) magnet wire. The magnet wire portion of the lead assembly is bent in a zig-zag fashion to accommodate differential thermal contraction between the cover plate and the radiation shield during cooldown.

The paired magnet wire extensions are soldered at their lower ends to 57.2 mm long by 12.7 mm wide copper blocks, shown in Fig. 2b. Each copper block is firmly clamped to the radiation shield upper plate. A 50.8 μm thick, electrically insulating Kapton sheet, coated on each side with a thin layer of Apiezon N grease, is inserted between each copper block and the radiation shield plate. This clamped connection thermally anchors the junction between the copper lead section and the HTS leads to the 1st stage of the cryocooler, both to control the upper operating temperature for the HTS leads and to limit the heat conducted through the HTS leads to the magnet.

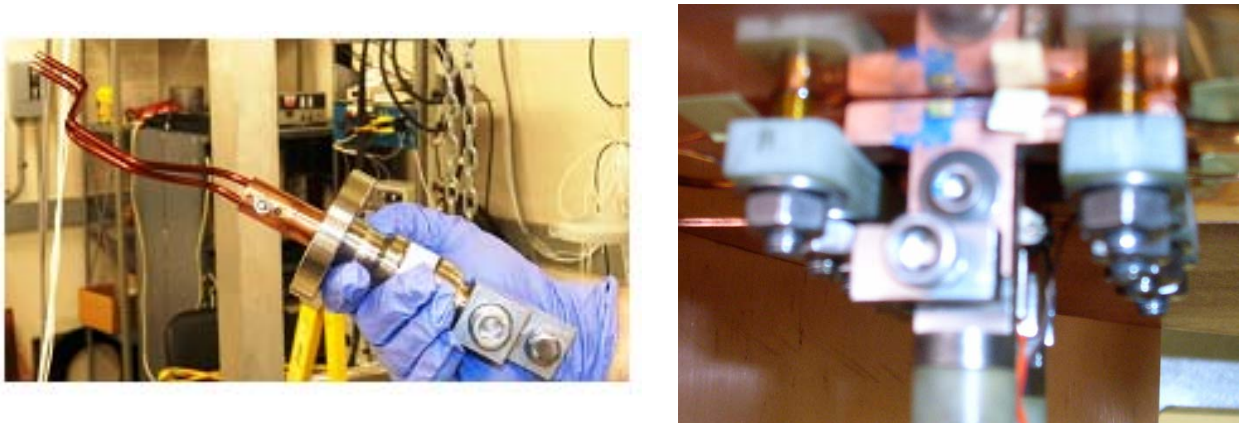

Fig. 2: Copper portion of current leads showing a) electrode clamp and zig-zag bending of the paired, 6AWG magnet wire extension, and b) thermal connection to the radiation shield and electrical connection to the HTS leads.

The lead thermal anchors at the radiation shield plate shown in Fig. 2b also provide the electrical connection between the copper and HTS lead sections. Because the magnet test setup is a temporary arrangement, we decided to use mechanically clamped joints so that the HTS leads could be readily reused for a subsequent, more permanent application. The use of mechanically clamped connections rather than soldered joints results in at least an order of magnitude higher resistance for these joints. The resistance of the clamped joints is minimized to the extent possible through the use of 9.5 mm tall by 6.4 mm thick stainless steel clamps, which apply significant additional clamping force to the joints. Thermal contraction between the clamps and

the joints during cooldown were accommodated by controlled flexure of the clamps as they were installed at room temperature.

The lower ends of the HTS leads were connected using similar, clamped joints (shown in Fig. 3) to the NbTi wires, which were soldered to the Nb_3Sn terminals during winding. The exposed ends of the NbTi wires were soldered to small copper blocks to facilitate clamping to the end of the HTS leads. Also shown in Fig. 3 is a flexible thermal link that was recycled from a previous magnet project. The link is pressed to one side of the HTS lead end, while the NbTi mounting block is pressed to the other. The second end of the thermal anchor is likewise clamped to the magnet chill plate through a 50.8 μm thick, electrically insulating Kapton sheet, coated on each side with a thin layer of Apiezon N grease. The small loop in the NbTi wires and the contoured profile in the thermal link accommodate differential thermal contraction between the magnet assembly and the radiation shield during cooldown.

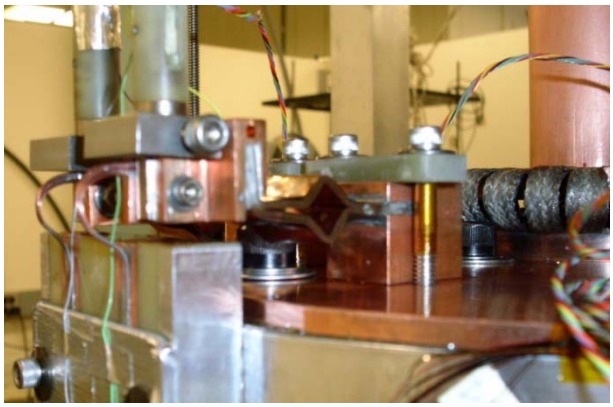

Fig. 3: Connection between lower end of HTS leads and the NbTi jumpers
(to the left of the image) and to the lower lead end thermal anchor (to the right).

Cooldown temperature monitoring: Fig. 4 shows the locations of the temperature sensors used to monitor the thermal performance of the test apparatus. Two types of temperature sensors were used. The temperatures of components attached to the 1st stage of the cold head were monitored using Lakeshore Cryotronics type DT-670 silicon diodes, which have roughly linear response with temperature. Four diode temperature sensors were used. The temperature at the 1st stage of the cold head was monitored by sensor T_{D1}, while that at the bottom of the radiation shield was monitored by sensor T_{D2}. The respective temperatures at the top of the left and right hand side HTS leads were monitored by sensors T_{D3} and T_{D4}.

The temperatures of components attached to the 2nd stage of the cold head were monitored using Lakeshore type CX-150-AA Cernox sensors. Five Cernox temperature sensors were used. The temperature at the 2nd stage of the cold head was monitored by sensor T_{C1}, while that at the magnet chill plate was monitored by sensor T_{C2}. The respective temperatures at the bottoms of the left and right hand side HTS leads were monitored by sensors T_{C3} and T_{C4}. The final sensor, T_{C5} was embedded in an aluminum spacer ring inside the iron yoke, immediately beneath the Nb_3Sn winding. The cold bus between the 2nd stage of the cryocooler and the magnet assembly was also equipped with a 135 Ohm cartridge heater that could be used to check the thermal response at the 2nd stage of the cold head as needed.

Assembly of the test apparatus was completed during the afternoon of Jan. 18, 2012 and was followed by evacuation of the test vessel, beginning at 18:00 that evening. By noon on Jan. 20, the pressure in the vessel had dropped to 4×10^{-4} Torr, at which point the cryocooler was switched on. Fig. 5 shows the cooling trends observed for all temperature sensors shown in Fig. 4.

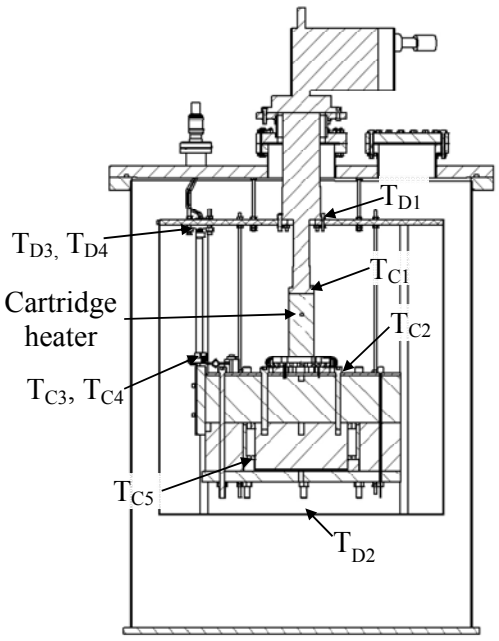

Fig. 4: Locations of temperature sensors used to monitor the thermal performance of the test apparatus.

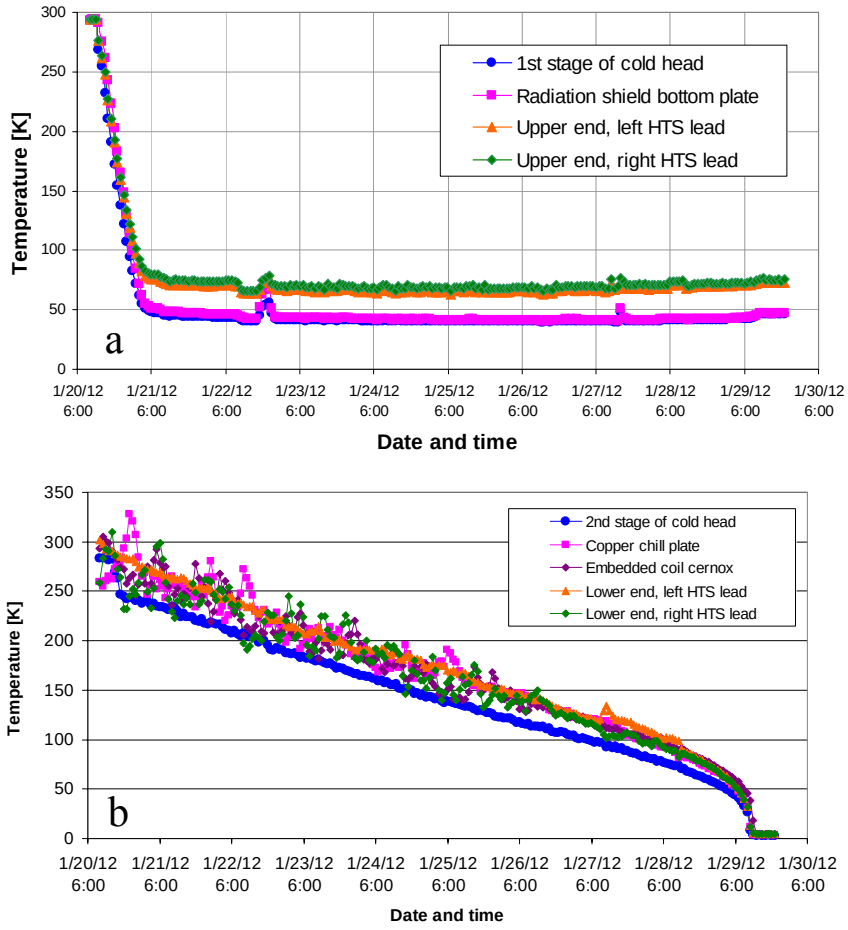

Fig. 5: Cooling trends observed with a) the silicon diode and b) Cernox temperature sensors.

The results in Fig. 5a indicate that all components attached to the 1st stage of the cold head achieved their near final temperatures within the first day of cooling. The measured temperature at the bottom of the radiation shield typically remained within one degree of that measured at the cold head, confirming the effectiveness of the MLI to limit the thermal radiation heat load on the shield. The measured temperatures at the thermal anchors at the upper ends of the HTS leads were approximately 28 degrees higher than that at the cold head, confirming that the conduction heat load along the copper portion of the leads was the dominant heat load on the 1st stage of the cold head. By the end of the cooldown, around noon on Jan. 30, the temperature at the cold head was 46 K. The temperature at the bottom of the radiation shield was 47 K, while the average temperature of the thermal anchors at the upper ends of the HTS leads was 74 K. During cooldown, the temperatures of the feedthrough electrodes outside the vacuum vessel were maintained at approximately 293 K by use of a pair of thermostatically controlled heaters, to prevent moisture condensation or ice buildup in the absence of current in the leads.

The results in Fig. 5b show that the components attached to the 2nd stage of the cold head took significantly longer to cool. This is not surprising given the significantly greater mass of the magnet assembly compared to that of the radiation shield, combined with the significantly lower heat removal capacity at the 2nd stage of the cold head. Cernox temperature sensors are resistance-temperature devices, with negative resistance versus temperature characteristics, which have rather poor sensitivity near room temperatures. The nominal resistance of the Cernox sensors near room temperature range from 70 Ohm to 80 Ohm. As the temperature drops towards 120 K their resistance increases to between 200 Ohm and 300 Ohm, while near 4K the sensor resistance values range from roughly 2000 Ohm to 5000 Ohm. For the cooldown sequence in Fig. 5b the excitation current to the Cernox sensor was set at a fixed value of 10 μA. The large scatter in the computed temperature readings for most sensors was caused by a few mV noise in the recorded signals. Note that the scatter in the readings decreases markedly as the temperature readings drop below roughly 150 K.

At the completion of the 2nd stage cold mass cooldown, around 09:00 on Jan. 29, the measured temperature at the 2nd stage of the cold head was 3.15 K. The measured temperature at the magnet chill plate was 3.58 K, while that at the sensor embedded below the coil was 3.80 K. The measured temperature at the bottom of the left HTS lead was 4.71 K, while that at the bottom of the right HTS lead was 4.80 K. By the time cooldown ended, the pressure in the test vessel was roughly 5×10^{-7} Torr.

Static heat loads: The three main heat loads on the test assembly, in the absence of magnet current, are: thermal conduction along structural supports and lead wires, thermal radiation, and residual gas heat transfer [4]. Table 2 summarizes the computed heat loads on each stage of the cold head based on the physical properties of the test apparatus and its measured temperature distribution. Residual gas heat transfer was virtually eliminated during the tests by maintaining the vessel pressure well below 10^{-4} Torr during cooldown, and does not appear in Table 2 [4].

Table 2: Static heat loads on the test apparatus at end of cooldown

Heat load	1st stage of cold head	2nd stage of cold head
Conduction along current leads	31.12 W	0.17 W
Conduction along ¼-20 support rods	1.38 W	0.01 W
Conduction along instrument leads	0.04 W	0.02 W
Thermal radiation	4.32 W	Negligible
	36.86 W	0.20 W

Thermal conduction along the copper section of both current leads to the radiation shield plate, $Q_{c,Cu}$, was determined by multiplying the ratio of the cross-sectional area to length of the leads by the integrated thermal conductivity for copper between room temperature (293 K) and the measured temperature at the radiation shield thermal anchors (74 K). Because of the change in cross-sectional area of the lead from that of the feedthrough electrode to that for the paired magnet wire extensions this calculation required an additional step, namely, the determination of the temperature, $T_j \sim 278.5$ K, at the junction between the copper lead sections.

$$Q_{c,Cu} = 2\frac{A_e}{L_e}\int_{T_j}^{293\ K} k_{Cu(T)dT} = 2\frac{A_{mw}}{L_{mw}}\int_{74\ K}^{T_j} k_{Cu(T)dT},$$

$$\text{where } k_{Cu} = 10^{\frac{2.2154-0.88068T^{0.5}+0.29505T-0.04831T^{1.5}+0.003207T^2}{1-0.47461T^{0.5}+0.13871T-0.02043T^{1.5}+0.001281T^2}}$$

A_e and L_e respectively are the cross-sectional area and length of the feedthrough electrode. A_{mw} and L_{mw} respectively are the combined cross-sectional area and length of the paired magnet wire extensions, and $k_{Cu}(T)$ is the temperature dependent thermal conductivity for a reasonably pure (100 RRR), commercial grade of copper [5]. The factor of 2 enters into the equation because there are two of these leads in the assembly.

Thermal conduction along the three ¼-20 support rods was determined similarly both for the radiation shield supports and for the coil supports. For this case, the root diameter of the thread was used to calculate the cross-sectional area of the rods, and the thermal conductivity for stainless steel, k_{ss}, was obtained from the NIST website [6]:

$$k_{ss} = 10^{a+b\ log(T)+c\log(T)^2+d\log(T)^3+e\log(T)^4+f\log(T)^5+g\log(T)^6+h\log(T)^7+i\log(T)^8}, \text{ where}$$
$$a = -1.4087, b = 1.3982, c = 0.2543, d = -0.6260, e = 0.2334,$$
$$f = 0.4256, g = -0.4658, h = 0.1650, \text{and } i = -0.0199.$$

The thermal radiation from the vacuum vessel walls to the radiation shield was estimated by multiplying the total surface area of the shield (1.96 m^2) by an assumed value of 2.2 W/m, which is typical for average, carefully applied MLI [7].

The 0.17 W value for thermal conduction along the HTS leads was obtained by linearly scaling the manufacturer's published value of 0.145 W for a pair of 500 A leads operating between 64 K and 4 K to the 74 K upper end and ~5 K lower end HTS temperatures measured for our setup [8].

Fig. 6 shows the thermal response of the test apparatus' Leybold cryocooler, measured in a standalone test in our laboratory on Nov. 14, 2011. For this test, each stage of the cryocooler was equipped only with a small heater mounted a short distance away from the lower side of the

stage and a temperature sensor mounted to the upper surface of the stage. Because we anticipated slightly larger heat loads than were actually observed in the magnet test setup, the majority of heat loads applied during the cold head characterization were biased towards higher values.

The solid black dot in Fig. 6 indicates the 46 K 1st stage and 3.15 K 2nd stage temperatures measured at the cold head following cooldown of the magnet test apparatus. The cold head's measured temperature versus heat load response in Fig. 6 suggests respective heat load values for the cold head stages of roughly 35 W for the 1st stage and 0.18 W for the second stage, which are in good agreement with the computed values summarized in Table 2.

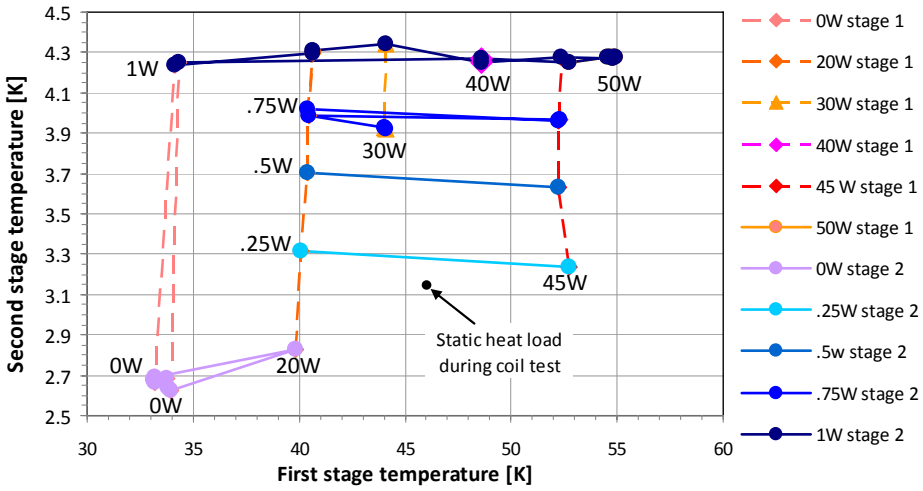

Fig. 6: Measured thermal performance of the Leybold cryocooler, overlaid with measured temperatures for the Nanotron coil test apparatus.

Thermal resistance of radiation shield thermal anchor: The 28 K temperature drop across the Kapton sheet that was used to electrically insulate the current leads from the radiation shield plate is significantly higher than anticipated. The large temperature drop is due in part to the larger than planned diameter of the copper lead wire extensions, which significantly increased thermal conduction along the leads, as well as our inability to locate a slightly thinner sheet of Kapton in time for this installation, which would have decreased the thermal resistance of the sheet.

The arrangement of the thermal anchor was modified in early January to eliminate an additional bolted interface. The 525.4 mm^2 contact area, A_K, between the Kapton sheet and the lead anchors was limited in part by the need to accommodate existing holes in the radiation shield plate. The anticipated temperature drop, ΔT_K, across the L_K = 50.8 µm thick Kapton sheet due to the 15.6 W heat load, Q_K, conducted from room temperature along each lead is given by:

$$Q_K = \frac{A_K}{L_K}\int_{74-\Delta T_K}^{74\,K} k_K(T)dT$$

where the thermal conductivity of Kapton is given by [9]:

$$k_K = 10^{a+b\,log(T)+c\,\log(T)^2+d\,\log(T)^3+e\,\log(T)^4+f\,\log(T)^5+g\,\log(T)^6+h\,\log(T)^7}, \text{ with}$$
$$a = 5.73101, b = -39.5199, c = 79.9313, d = -83.8572, e = 50.9157,$$
$$f = -17.9835, g = 3.42413 \text{ and } h = 0.1650.$$

Solving this equation for ΔT_K yields an expected temperature drop across each Kapton sheet of roughly 13 K.

Due to the high local heat load at the lead anchor location it is reasonable to expect a similar temperature drop between the lead anchor location and the 1st stage of the cold head. Approximating the width of this thermal path, $w_{Sh} = 106.7\ mm$, as equal to the diameter of the cold head stage, and the conduction path length, $l_{Sh} = 182.9\ mm$, as equal to the average distance between the thermal anchors and the stage, yields an estimated temperature drop along the top plate of the radiation shield of $\Delta T_{Sh} \sim 4\ K$.

Our best estimate of the temperature difference between the lead anchors and the 1st stage of the cold head can account for only 17 K of the measured 28 K difference. Possible explanations for this discrepancy are that not all of the apparent areas of contact between the thermal anchor, Kapton sheet and the radiation shield is effectively included in the heat transfer path, or that there exists an additional thermal contact resistance at the interface between the thermal anchor, Kapton sheet and the radiation shield that adds to the measured temperature drop.

Magnet excitation experiments: Fig. 7 presents a partial section view of the test apparatus, showing the locations of the voltage taps that were installed along the current leads to monitor the performance of each lead section. Fig. 7 also indicates the location of a Hall probe sensor that was located in a small gap between the yoke pole tip and yoke bottom plate. This sensor was used to record the variation in magnetic field near the pole tip versus the coil excitation current.

Eight voltage taps were installed inside the test vessel. These were symmetrically placed along each of the two current leads. The voltage taps labeled V_{L1} and V_{R1} were installed at the bolted connection between the feedthrough electrodes and the magnet wire portion of each lead. The voltage taps labeled V_{L2} and V_{R2} were installed at the bolted connection between the lead thermal anchors and the upper ends of the HTS leads. The voltage taps labeled V_{L3} and V_{R3} were installed at the bolted connection between the lower ends of the HTS leads and the NbTi lead wires attached to the terminals of the Nb_3Sn winding. The voltage taps labeled V_{L4} and V_{R4} were also installed on the NbTi lead wires at the point where they entered the iron yoke.

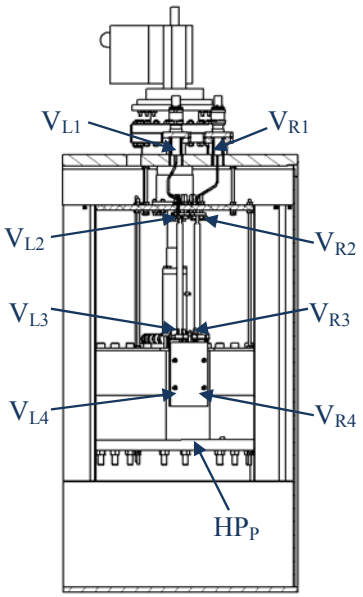

Voltage tap pairs monitored in data acquisition system

Voltage tap pair	Monitored signal
$V_{L2} - V_{L1}$	Left copper lead section
$V_{R1} - V_{R2}$	Right copper lead section
$V_{L3} - V_{L2}$	Left HTS lead
$V_{R2} - V_{R3}$	Right HTS lead
$V_{L4} - V_{L3}$	Left NbTi jumper
$V_{R3} - V_{R4}$	Right NbTi jumper
$V_{R4} - V_{L4}$	Voltage across Nb_3Sn winding

Fig. 7: Partial section view of the test apparatus showing the locations of voltage taps and Hall probes that monitor the system performance during the magnet excitation experiments.

Pretest analysis of the conductor and magnet properties indicated that, within the constraints imposed by the winding insulation and instrument feedthrough voltage rating, the magnet system could be protected against quench damage up to an operating current of roughly 200 A [10]. Quenching refers to the unplanned transition of a portion of the winding from the superconducting to the resistive state. If the resistive zone were to spread quickly enough the stored magnetic energy could be safely dissipated through the entire winding volume, otherwise some means would need to be devised to safely dissipate the winding's stored magnetic energy outside of the winding volume. The pretest quench analysis for the Nanotron prototype magnet test indicates that, because of the thickness of the S-2 glass insulation, resistive zones in the winding grow very slowly and we would need to begin to dissipate the winding's stored energy outside of the magnet assembly within 20 ms of the detection of a quench voltage greater than 50 mV [10]. For completeness, a copy of the quench analysis report is included as Appendix A. The implementation of an accurate and fast acting quench detection for this single coil system was complicated by the absence of voltage taps within the winding volume and by the non-linearity in coil inductance caused by its incorporation with an iron yoke. A voltage tap installed near the center of the winding is typically used for this type of magnet system so that inductive voltages from one half of the winding can be balanced against those from the other, with any subsequent imbalance signal being attributed to a quenching resistive zone.

Fig. 8 shows a schematic of the current source and quench protection circuit assembled for the magnet excitation tests. Energization for the tests was provided by a 0~10 V, 0~1000 A PowerTen series 4700 DC power supply. The supply was connected through a fast acting IGBT switch to the magnet assembly. An 0.9 Ohm custom-built resistor was connected across the coil terminals to permit the magnet's stored energy to be dissipated outside of the test vessel in the event a quench was detected. The current through the magnet was measured using a calibrated resistor mounted in the magnet's current return. A 3.6 V diode was installed across the power supply terminals to protect the supply from possible voltage spikes that might occur if the IGBT switch opened with the magnet at high current.

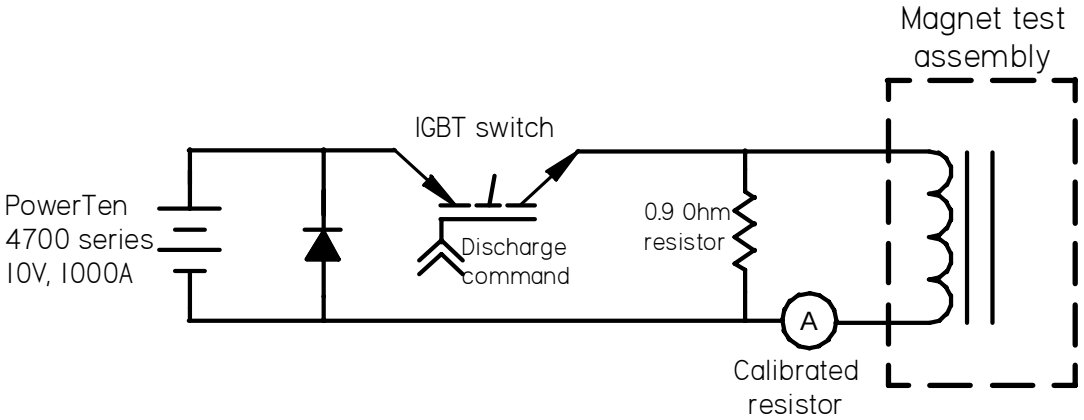

Fig. 8: Schematic of the current source and protection circuit used for the magnet excitation tests.

The coil was subjected to roughly ten energization cycles, occurring on Feb. 1 and Feb. 2, 2012. The first, approximately half dozen cycles were limited to peak currents in the range from 50 A to 100 A, and were performed on Feb. 1 to verify the operation of the data acquisition and system protection monitoring systems. The tests on Feb. 2 employed progressively increasing peak currents that were designed so that the stored energy in the magnet roughly doubled from

one test to the next. The test sequence ended with an apparent quench at 236 A that was detected, but not quickly enough to prevent damage to the coil during the fast energy discharge.

Representative results from the 211 A excitation test: Fig. 9 shows the variation in magnet current versus time for the magnetization energization test to 211 A peak current. Above about 20 A the current ramp rate is nearly linear, with a slope of roughly 0.51 A/s. The magnet has a very large effective inductance at low current because of the initial magnetization of the iron yoke; the corresponding charging voltage limits current output from the power supply and distorts the current versus time profile in Fig. 9 at currents below roughly 20 A.

Table 3 summarizes results from a VectorField model of the magnet assembly and shows the expected variation in stored the magnetic energy and magnetic induction at the Hall probe location near the pole tip at various operating currents [11]. Fig. 10 compares the computed magnetic induction at the pole tip at various currents to the measured values. The match between computation and measurements is surprisingly good considering the anticipated +/-3% variation in Hall probe sensitivity between the calibration value obtained at room temperature and its 4 K operating temperature, and the expected variation between the simulated and actual magnetic properties of the yoke, which can depend on use temperature, chemical composition and process history [12].

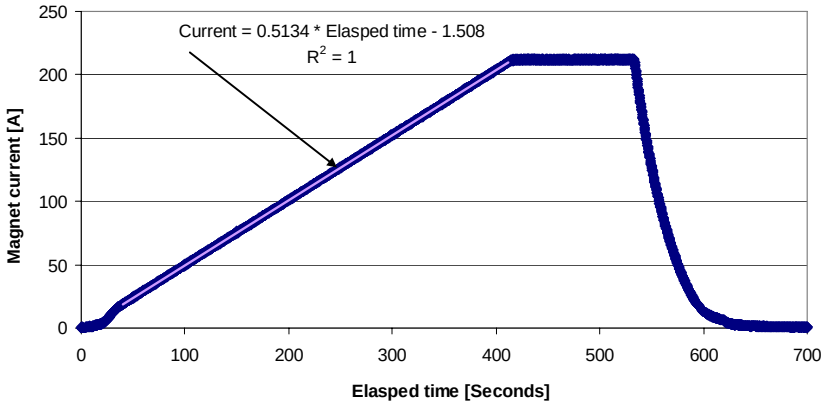

Fig. 9: Current versus time for the magnet excitation experiment to 211 A peak current.

Table 3: Computed magnetic energy and pole tip magnetic induction at various currents

Magnet current [A]	Stored energy [J]	Pole tip magnetic induction [T]
1	10.7	0.35
4	109.2	0.99
5	139	1.05
10	280	1.20
25	577	1.40
50	1328	1.75
75	2501	2.02
100	4090	2.22
150	8442	2.51
200	14267	2.78
211	15706	2.83
236	19280	2.96

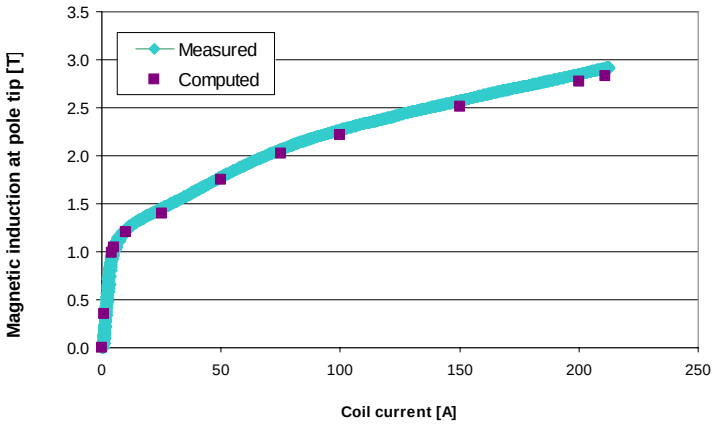

Fig. 10: Computed and measured pole tip magnetic induction versus current for the magnet assembly.

Fig. 11 shows the measured and computed variation in the coil voltage versus current for the 211 A test. The computed voltages, V_r, during the current upramp were obtained by multiplying the effective coil inductance, $L_e(I_a)$, by the instantaneous current ramp rate, dI_a/dt. Below 20 A the current ramp rate was obtained using a 6th order fit of the data, whereas above 20 A a fixed ramp rate value of 0.51 A/s was used.

$$V_r = L_e(I_a)\frac{dI_a}{dt}.$$

The effective inductance was obtained by first subtracting adjacent stored magnetic energy values in Table 3, E_i, and then dividing twice this value by the difference between the squares of the corresponding coil currents, I_i^2. Because the stored energy in the magnet varies as the square of the coil current is it perhaps more appropriate to set I_a to the geometric, rather than the arithmetic average of the adjacent current values.

$$L_e(I_a) = \frac{2(E_2-E_1)}{(I_2^2-I_1^2)}, \text{ with } I_a = \sqrt{I_1 I_2}.$$

Note that the measured coil voltage progressively decreases with increasing coil current. Thus, although the signal was reasonably free from noise, comparison of the coil voltage signal against a fixed quench detection threshold that is set roughly 50 mV greater than the coil voltage observed at 50 A, permitted an gradually increasing gap between the desired and achievable quench detection signal as the coil current increased at fixed ramp rate.

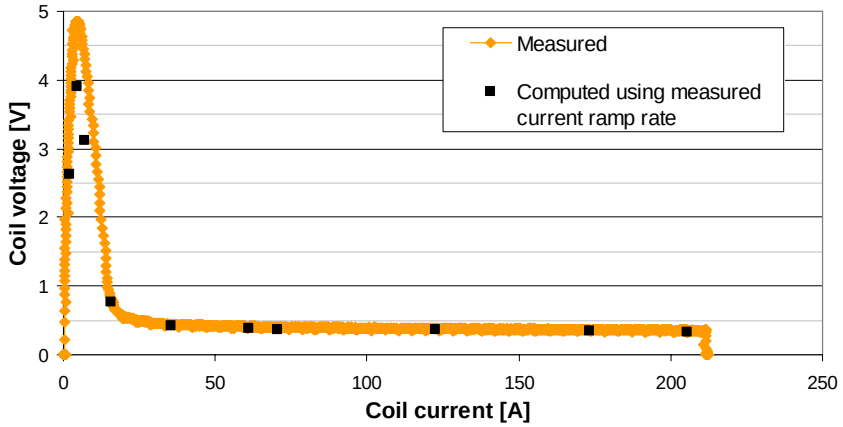

Fig. 11: Measured and computed coil voltage versus current for 211 A test.

Fig. 12 shows the measured variation in current lead voltages versus coil current for the 211 A test. Fig. 12a shows the variation in measured voltages for the copper sections of the leads, while Fig. 12b shows the variation in measured voltages for the HTS and NbTi lead sections. Both lead sections of a given type show quite similar variation with current. The voltage drop for the left copper lead section increases from zero to 10.6 mV, while that for the right copper lead section increases to approximately 10.4 mV as the coil current rises to 211 A; the corresponding power dissipation in each copper lead section is roughly 2.2 W, which is well within their designed operating limits.

The measured voltage drop along each HTS lead section in Fig. 12b is dominated by the resistance of the clamped joints at both ends of the lead. The measured voltage at 211 A for the left HTS lead was 1.0 mV, while that for the right HTS lead was 0.8 mV; the average power dissipation at each clamped joint is in the range between 84 mW and 105 mW, assuming that joints at the upper and lower ends of the leads have roughly equal resistance. As expected, the voltage drop along the soldered, NbTi lead sections remain vanishingly small, indicating that this part of the lead remains fully superconducting and that soldered joints to the terminal blocks attached to the HTS leads have negligible electrical resistance.

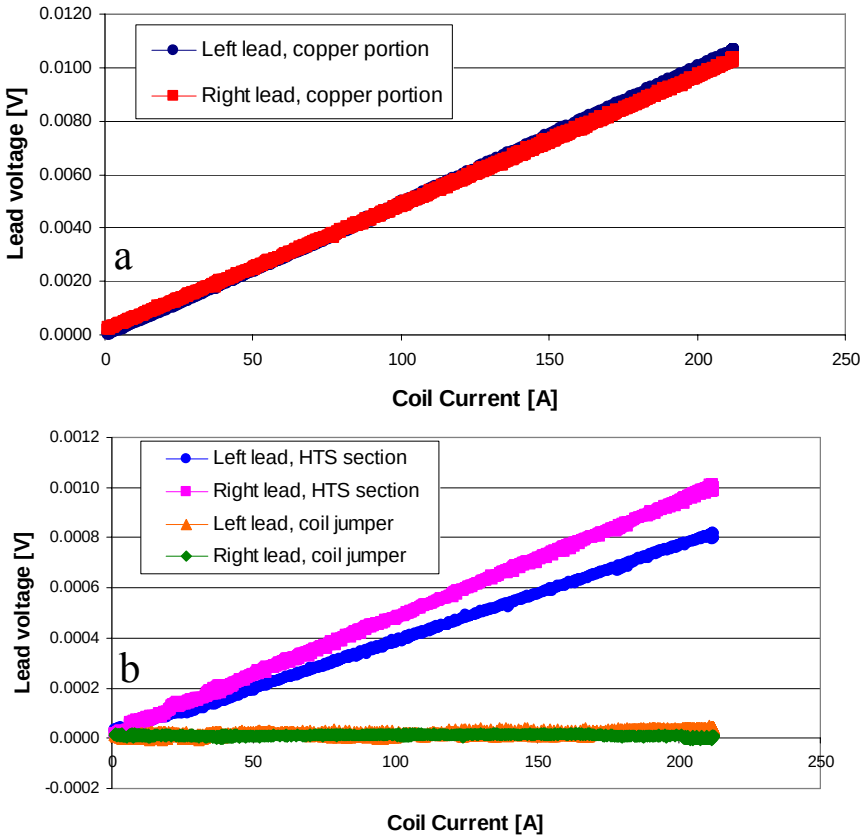

Fig. 12: Variation in measured voltage drops along the a) copper lead and b) HTS and NbTi lead sections versus current during the 211 A tests.

Fig. 13 shows the measured variation in temperature for components connected to the 2nd stage of the cold head during the 211 A current excitation test. Unfortunately, the diode temperature sensors showed quite pronounced coupling with the power supply output, which made it impossible to extract meaningful data from the 1st stage temperature sensors during the current excitation tests. Extensive post-test examination of the sensor lead wire resistances indicate that the sensor leads are not shorted to either the vessel or to the coil. Based on the manufacturer's product literature we conclude that ac noise pick-up in the lead wires was responsible for the observed discrepancies in the diode temperature sensor measurements [13].

The measured temperatures at the lower end of the HTS leads in Fig. 13 show roughly quadratic variation with current, consistent with resistive power dissipation in the clamped joints between the HTS and NbTi lead sections as noted above. The 2nd stage cold head temperature readings presented in Fig. 13 were recreated using signals logged by the protection system PLC, which recorded data at a 10 s sampling rate; the cold head signal was inadvertently omitted from the data acquisition record. The longer sampling interval for the 2nd stage cold heat temperature readings accounts for the relatively wide spacing between adjacent data points. The temperature reading at the 2nd stage of the cold head increased from its steady, no-load value of 3.15 K to roughly 3.45 K, observed towards the end of the 211 A flattop current hold. According to Fig. 6, the 3.45 K 2nd stage temperature corresponds to a heat load of roughly 0.38 W. The 0.20 W increase in 2nd stage heat load is consistent with the combined, average joint resistance heating at the lower ends of the HTS leads deduced from the voltage measurements in Fig. 12b.

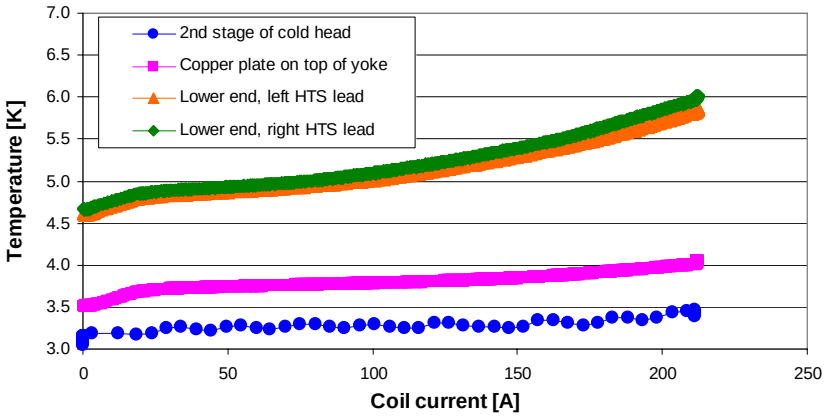

Fig. 13: Variation in measured temperature for components attached to the 2nd stage of the cold head versus current during the 211 A magnet excitation tests.

236 A quench: Fig. 14 shows the coil current and coil voltage traces versus time for the final run of the test sequence. The programmed current upramp was abruptly terminated by a quench of the coil's superconductivity occurring at 236 A.

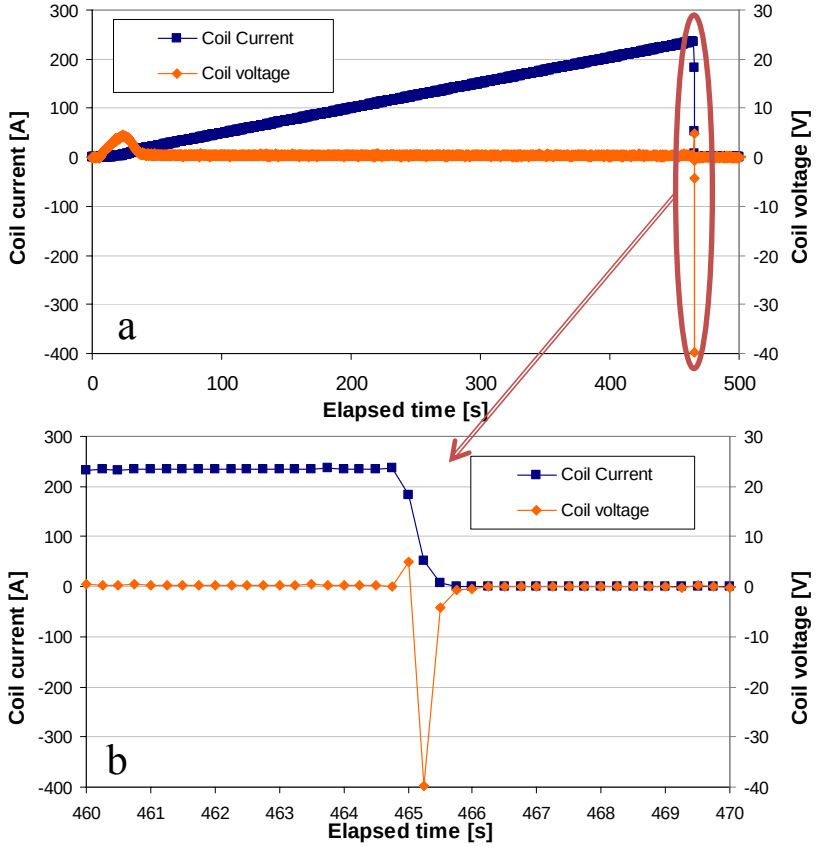

Fig. 14: Current and voltage versus elapsed time during the test ending in quench.
a) Full data trace and b) expanded time trace showing details of the quench event.

The horizontal axis in Fig. 14a shows the elapsed time for the entire current ramp, while the horizontal axis in Fig. 14b is expanded to highlight the rapid changes in coil current and voltage observed during the quench. The total duration for initiation, detection and active discharge of the coil current through the 0.9 Ohm resistor lasted roughly 1 s; this amounts to roughly four measurement intervals, at the data acquisition system's 0.25 s sampling rate.

Prior to the start of the current upramp, the quench detection voltage was set to a value of 0.48 V for coil currents greater than 50 A. Initial blanking of the quench detector was necessary in the present test arrangement to prevent inadvertent discharge of the coil current during the large inductive voltage transient that occurs near the start of each current upramp (below roughly 50 A in Fig. 11). The 0.48 V detection threshold was selected, according to the simulations in [10], to be roughly 50 mV larger than the instantaneous, 0.43 V inductive coil voltage observed at 50 A in Fig. 11. However, by the time the coil current reached 236 A in Fig. 14a, the inductive coil voltage had dropped to approximately 0.33 V, resulting in a significantly higher than proposed detection threshold, with a value of approximately 150 mV.

The net coil voltage during the quench consists of both a resistive and an inductive component. The first data point during the quench (at 465 s elapsed time in Fig. 12b) shows a net

positive, 5.2 V coil voltage despite a significant drop in coil current to below 200 A, that is, the resistive voltage component dominates during the early stages of the quench. As the IGBT switch in Fig. 8 opens and the coil current is dissipated in the external 0.9 Ohm resistor, the current discharge rate increases and the inductive voltage dominates, resulting in a net negative -42.6 V discharge voltage across the coil terminals. If the quench had been detected sooner, the initial resistive voltage rise would have been insignificant, while the peak discharge voltage would have been several times larger.

Fig. 15 shows the temperature variation during and after the quench for components attached to the 2nd stage of the cold head. The temperature of all components attached to the yoke show similar variation, with peak temperatures of approximately 20 K. Because the total mass of the magnet assembly is nearly the same as that of the iron yoke, the total energy dissipated in the magnet assembly during the quench, E_m, can be roughly estimated based on the total mass of the yoke, m_y, the yoke's temperature dependent heat capacity, $C_{p,y}(T)$, the temperature immediately before the quench, $T_{y,i}$, and the measured peak temperature, $T_{y,p}$.

$$E_m = m_y \int_{T_{y,i}}^{T_{y,p}} C_{p,y}(T)\ dT$$

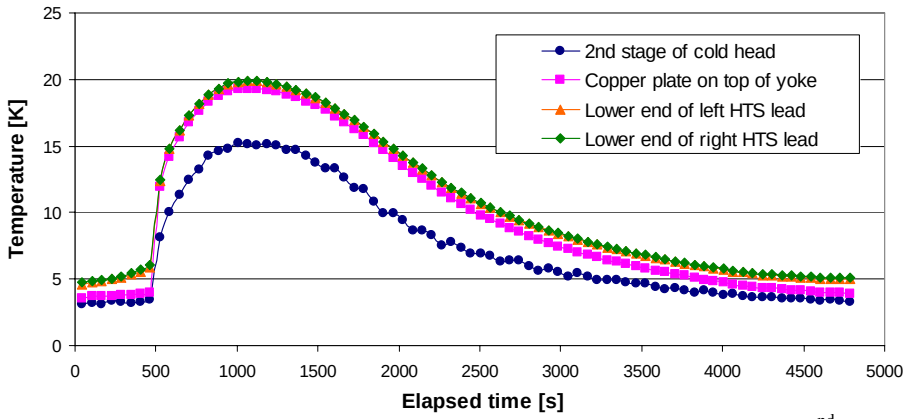

Fig. 15: Variation in measured temperature for components attached to the 2nd stage of the cold head versus elapsed time during and following the 236 A quench.

For this approximation, the yoke temperature was set equal to that measured for the copper chill plate, while the temperature dependent heat capacity data was taken from Table 1 in [14]. The estimated energy dissipation in the magnet assembly during the quench is approximately 7.5 kJ, which is roughly 40% of the stored magnetic energy listed in Table 3 for the coil at 236 A operating current. Because the normal zone during quench does not spread significantly [10], it is not surprising that such a large local deposition of energy could damage the coil. Despite the large value of the energy dissipated in the magnet assembly, the time required to return to its initial, "no-load" temperature distribution is just over an hour. Attempts to charge the coil following this recool time produced a resistive response. Subsequent measurement using a hand-held multimeter confirmed roughly 1 kOhm coil resistance across the test apparatus current leads.

Warmup temperature monitoring: The Leybold cryocooler was switched off at 15:00 on Feb. 2, following the conclusion of the magnet excitation tests. Fig. 16 shows the temperature trends measured as the test apparatus warmed back towards room temperature. Fig. 16a shows the warmup data for components attached to the 1st stage of the cold head, while Fig. 16b shows the

warmup data for components attached to the 2nd stage of the cold head. Note that the noise for the Cernox sensor readings above roughly 150 K (in Fig. 16b) is significantly smaller than that for the cooldown measurements in Fig. 5b; this was achieved by increasing the sensor current from 10 μA, used at low temperatures, to 100 μA.

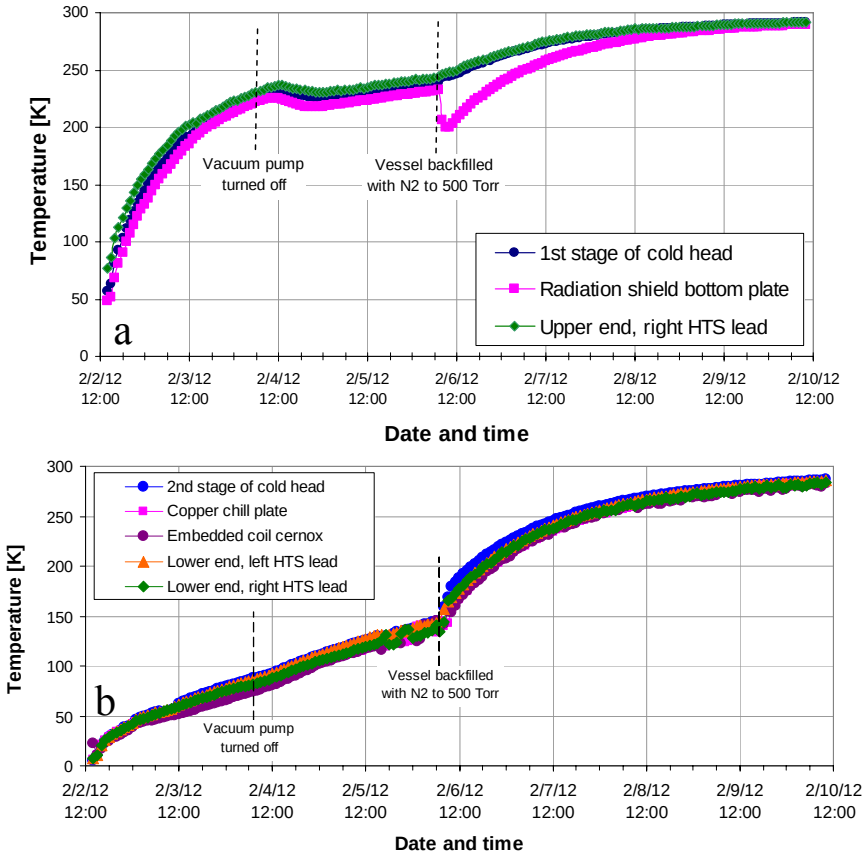

Fig. 16: Warmup trends observed with a) the silicon diode and b) Cernox temperature sensors.

Several steps were taken to help speed the warmup process. The cartridge heater installed in the cold bus attached to the 2nd stage of the cold head was energized to a heating power of roughly 4.5 W from the start of the warmup and remained energized until data recording was terminated around noon on Feb. 10. The vacuum vessel pump-out valve, which had remained closed since the end of the cooldown was reopened, and the vacuum pump was restarted; this was done to remove any species, specifically any helium or hydrogen, which might outgas from the cryogenically cold surfaces of the vessel as they warmed. Around 09:00 on Feb. 4, after the temperature of the magnet mass had risen above roughly 80 K, the vacuum pump was shut off, allowing the pressure in the vessel to rise as the cold components continued to outgas higher molecular weight species. Because this operation occurred during the weekend, the vacuum could not be fully broken with dry nitrogen gas until technicians were available during the morning on Feb. 6. Around 09:00 on Feb. 6 the pressure in the vessel was increased from roughly 30 mTorr to 500 Torr by introduction of dry nitrogen.

The effect of changes to the vessel pressure is readily observed in Fig. 12. Turning off the vacuum pump markedly slowed the warming of the 1st stage cold head components, while the warming of 2nd stage components continued at a slightly accelerated rate despite their continually

increasing heat capacity. Convective heat transfer from the radiation shield to the magnet assembly due to the presence of outgassed species was at least partially effective to speed the magnet's warming trend. This process was further accelerated by the large pressure increase imposed on Feb. 6, where convective transfer was strong enough to initially pull the temperature of the radiation shield close to that of the magnet assembly, and to simultaneous increasing the magnet's instantaneous warmup rate by a significant factor.

Conclusion: A small, conduction-cooled Nb_3Sn superconducting coil was tested in a 270 kg, A36 iron yoke during the week of Jan. 30, 2012. The results demonstrate the technical feasibility to routinely design, manufacture and operate this type of system at currents in excess of 200 A.

The test results emphasize the necessity to design and construct a magnet system with an eye towards quench detection. The inclusion of a voltage tap near the center of the Nb_3Sn winding for this standalone coil test would have greatly simplified our quench detection efforts and would likely have protected the winding from damage during the test sequence. Visual examination of the prototype Nb_3Sn winding following warming to room temperature confirmed the existence of two, small, closely-spaced sections of vaporized conductor at the inner bore of the winding, immediately adjacent to its upper, aluminum flange.

Heat generation at the joints to the upper and lower ends of the HTS leads can be significantly reduced in production devices by the use of soldered, rather than mechanically clamped joints at these locations. This contention is supported by the lack of any observable voltage across the soldered joints to NbTi lead sections during the current excitation tests.

The tests also highlight one area where further development is desirable, namely the investigation of methods that can substantially reduce the temperature difference between the copper lead section's thermal anchor and the 1^{st} stage of the cold head. Various methods such as reducing insulator thickness, increasing its apparent area of contact, altering the clamping method, or use of alternate insulators could be tried. This development effort could be implemented, for instance, with fairly quick turnaround of results, using a stand-alone current lead test stand connected to a cryocooler, without need for simultaneously cooling, testing and warming a full magnet system.

References

1. S. Pourrahimi, "Coil delivery," *Superconducting Systems, Inc. report*, Billerica, MA, 29 Aug. 2011.

2. A.F. Zeller, J.C. DeKamp, E.M.W. Leung and R.W. Fast, "Long term results from the elimination of MLI between 4 and 77 K," *Adv. Cryo. Eng*. **39** (1994) pp. 1691-1697.

3. R. McFee, "Optimum input leads for cryogenic apparatus," *The review of scientific instruments,* Vol. 20, Feb. 1959, pp. 98-102.

4. G. White, *Experimental techniques in low-temperature physics,* Oxford University Press, New York, 1987.

5. http://cryogenics.nist.gov/MPropsMAY/OFHC%20Copper/OFHC_Copper_rev.htm

6. http://cryogenics.nist.gov/MPropsMAY/304Stainless/304Stainless_rev.htm

7. A. Zhukovsky, "MLI system for LDX F- and L- cryostats," LDX project report *LDX-MIT-AZ-022601*, MIT, Cambridge, MA, 26 Feb. 2001.

8. http://www.hts110.co.nz/wp-content/uploads/2008/11/hts-110currentleads1.pdf

9. http://cryogenics.nist.gov/MPropsMAY/Polyimide%20Kapton/PolyimideKapton_rev.htm

10. B. Smith, "Quench Analysis of the Second Nanotron Test Coil," Nanotron project memo *Nanotron-MIT-BASmith-011912*, MIT, Cambridge, MA, 19 Jan. 2012.

11. A. Radovinsky, "Nanotron test coil magnetic analyses," Nanotron project memo *Nanotron-MIT-ARadovinsky-120208-01*, MIT, Cambridge, MA, 8 Feb. 2012.

12. R.M. Bozorth, *Ferromagnetism*, John Wiley and Sons, Hoboken, NJ, 2003.

13. Lake Shore Cryotronics Inc, "Appendix B: Sensor Characteristics," *Temperature measurement and control catalog* (2004) p.156.

14. P.D. Desai, Thermodynamic properties of iron and Silicon, *J. Phys. Chem. Ref. Data*, **15** (1986) pp. 967-983.

Memorandum

TO: Joe Minervini, Phil Michael
CC: Alexi Radovinsky, Craig Miller
FROM: B.A. Smith
DATE: January 19, 2012
SUBJ: Quench Analysis of the Second Nanotron Test Coil
REF: Nanotron-MIT-BASmith-011912

Executive Summary

An earlier memo[1] reported results of quench analyses completed on the first Nanotron test coil. A second Nanotron test coil has now been fabricated by Superconducting Systems Inc. (SSI) from an earlier generation of ITER Nb3Sn strand[2]. The SSI letter provides the key dimensions of the completed winding, which is housed inside an aluminum shell and is fitted with NbTi leads. The Nb3Sn-NbTi joint is protected by bolt-on aluminum splints which leave only the NbTi leads exposed. A data sheet for the Nb3Sn strand used in the winding is included with the SSI letter showing a measured Jc of 655 and 659 A/mm^2 (12 T, 4.2 K) at the two ends of the strand, corresponding to a nominal Ic of 141.5 A. The winding strand is insulated with a thin layer of S2 glass which is impregnated with epoxy after reaction. The SSI letter indicates that residual carbon from the insulation sustained during the wind and react heat treatment of the Nb3Sn winding has reduced the room temperature coil resistance from an expected 47 ohms to 19 ohms since the carbon provides a distributed resistance between the strand and the aluminum shell. This feature will likely prevent the coil from safely operating at high voltages during quench.

This memo reports on the quench analyses conducted on the second test coil. After discussion with Phil Michael and in consideration of the presence of the carbon in the winding, it was agreed to limit the allowable quench voltage to about 200 V. This quench protection voltage limit is significantly more limiting on the test coil operating current than would be otherwise be possible if higher voltages could be safely sustained on the winding. Stability analysis indicates that the operating current could be about 340 A while retaining a 1 K temperature margin at the peak field point of 6.22 T (see Fig. 1). With the 200 V limitation, however, the quench analysis indicates an operating current of 200 A is acceptable, but it requires fast quench detection and protection. The quench analysis assumes a 1 Ω dump resistor, a 50 mV quench detection threshold and a 20 ms time delay before protection is initiated. With these parameters, quench from 200 A results in a peak hot spot temperature of 123 K. The maximum winding voltage, 200 V, occurs at the terminals when the dump is initiated. Because of the small transverse thermal conductivity of the winding and the relatively small copper stabilizer cross section, the quench propagates very slowly. Only 5% of the winding is normal at the end of the transient. Because most of the winding is still cold, the small, locally hot region is in approximate hydrostatic compression, so winding stresses due to differential temperatures are not expected to be an issue.

[1] B.A. Smith, "Quench Analysis of the Nanotron Test Coil", July 25, 2011, Nanotron-MIT-BASmith-072511
[2] Shahin Pourrahimi, letter "Coil Delivery" to T.A. Antaya, August 29, 2011

Details

Parameters of the second test coil winding, as extracted from the SSI letter, are given in Table 1.

Table 1 Nanotron Test Coil 2

Parameter	Units	Value
Winding ID	inches	8.21
Winding OD	inches	9.675
Coil width	inches	2.425
Nlayers		22
Turns per layer		63
Al case ID	inches	8.21
Al case OD	inches	10.25
Al case width	inches	3.27
Strand diameter	mm	0.81
Cr coating thickness	micron	2
Wire diameter with S2 glass insulation	mm	9.62
Stored energy at 200 A	kJ	13.5

A Summers[3] fit was applied to a combination of data for this wire. Although better fits[4] are now available for the current generation of ITER strand, such fits have apparently not been made for this earlier generation of strand, so the somewhat simpler Summers fit was used here. A Kramer fit was made to data from Goodrich[5] to get the Bc20m value assuming a nominal strain of -0.0027, Tc0m was set at 16.3 K, and C0 was adjusted to give 141.5 A at 12 T, 4.2 K, -0.0027. The strain state in the wound configuration was taken as -0.004 based on an educated guess, given that the winding is thermally compressed at 4 K by the Al mandrel. A set of Ic(B, 4.2K, ε) plots with the current-field load line is shown in Fig. 1. Also shown for reference are two temperature margin operating points, one at 1 K and another at 1.5 K. As a point of interest, stability was examined against Eckels[6] stability parameter, which requires the length of the minimum propagating zone to be at least two conductor diameters. It is interesting to note that this stability limit is close to the 1 K temperature margin operating point. It is clear that were it not for the quench protection voltage limitation on this winding, higher operating currents, perhaps near 340 A, might be feasible while still achieving reasonable superconductor stability. However, with the imposed 200 V limit, after a few trial quench runs, operating current was set at 200 A with a 1 Ohm dump resistor, a 50 mV quench detection threshold and a 20 ms time delay.

Post-processed graphic output from the quench analysis is presented in Figs. 2-7. With the normal zone resistive voltage peaking at only ~1.5 V and with the confined geometry, the

[3] L.T. Summers, et al., A Model for the Prediction of Nb3Sn Critical Current as a Function of Field, Temperature, Strain and Radiation Damage, IEEE 'IRANSACTIONS ON MAGNETICS, VOL. 27, NO. 2, MARCH 1991, p. 2041

[4] L. Bottura, Jc(B,T,ε) PARAMETERIZATION FOR THE ITER Nb3Sn PRODUCTION, presented at Applied Superconductivity Conference 2008 (ASC 2008)
17-22 August 2008, Chicago, USA, 01 March 2009

[5] L. Goodrich, GoodrichIGC.ppt,

[6] P.W. Eckels, "Designing for Superconductor Magnet Stability Using Minimum Propagating Zone Theory", IEEE TRANSACTIONS ON MAGNETICS, VOL. 25, NO. 2, MARCH 1989, pp. 1706-1709.

voltage as a function of turn count is linear (no internal peaking) and will be a maximum of 200 V at the time the dump is triggered.

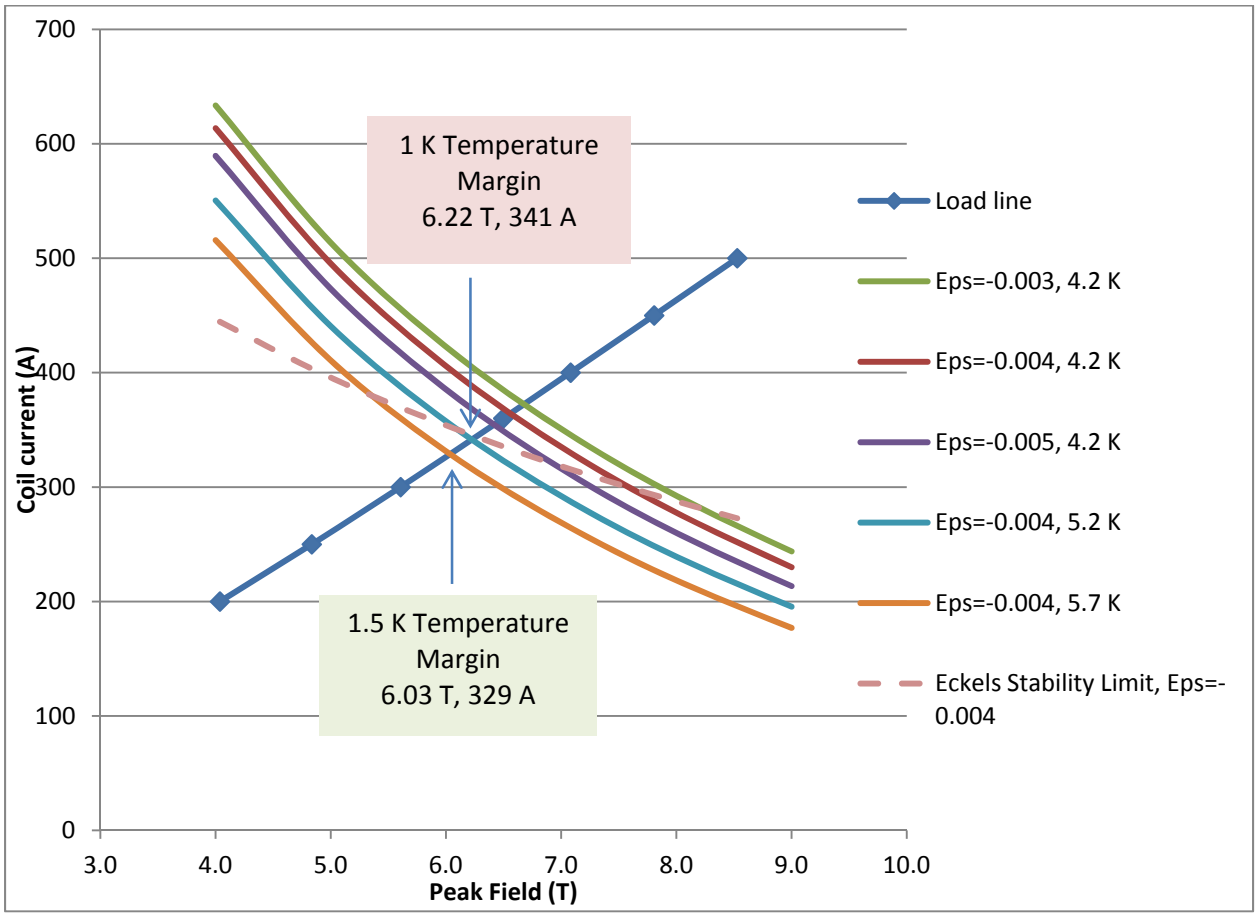

Fig. 1 Ic(B, 4.2K, ε) with Load Line. Eckels stability limit is also shown.

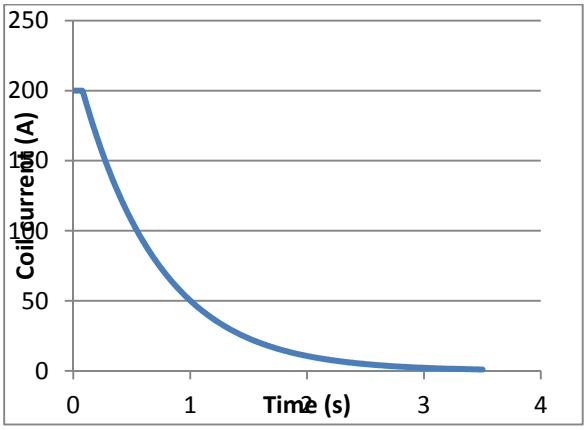

Fig. 2. Coil current

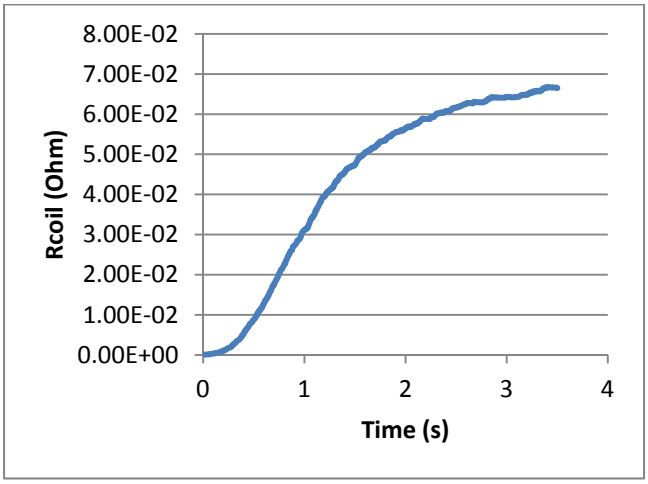

Fig. 3 Coil resistance

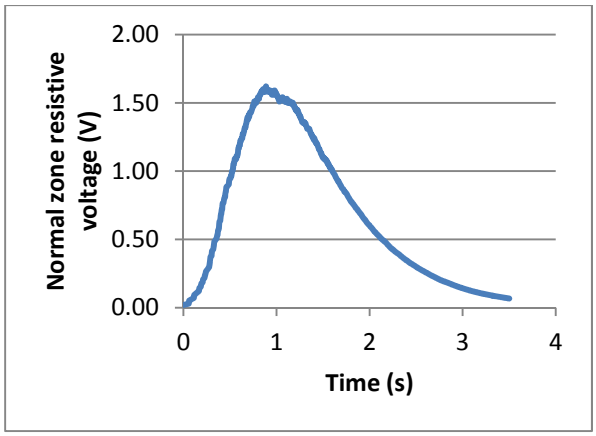

Fig. 4 Coil normal zone resistive voltage

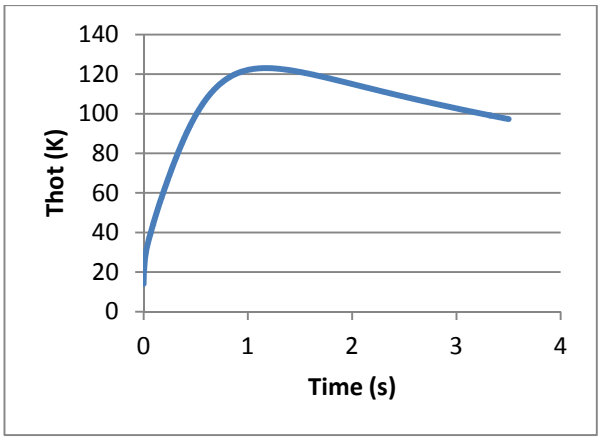

Fig. 5 Coil Hot Spot Temperature

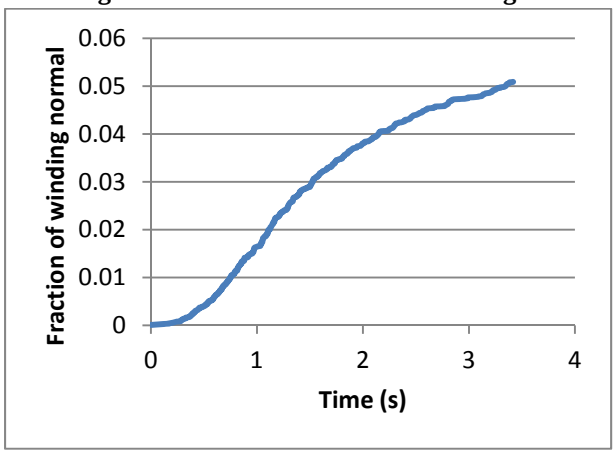

Fig. 6 Fraction of winding normal. Note that only 5% of the winding is normal at the end of the transient.

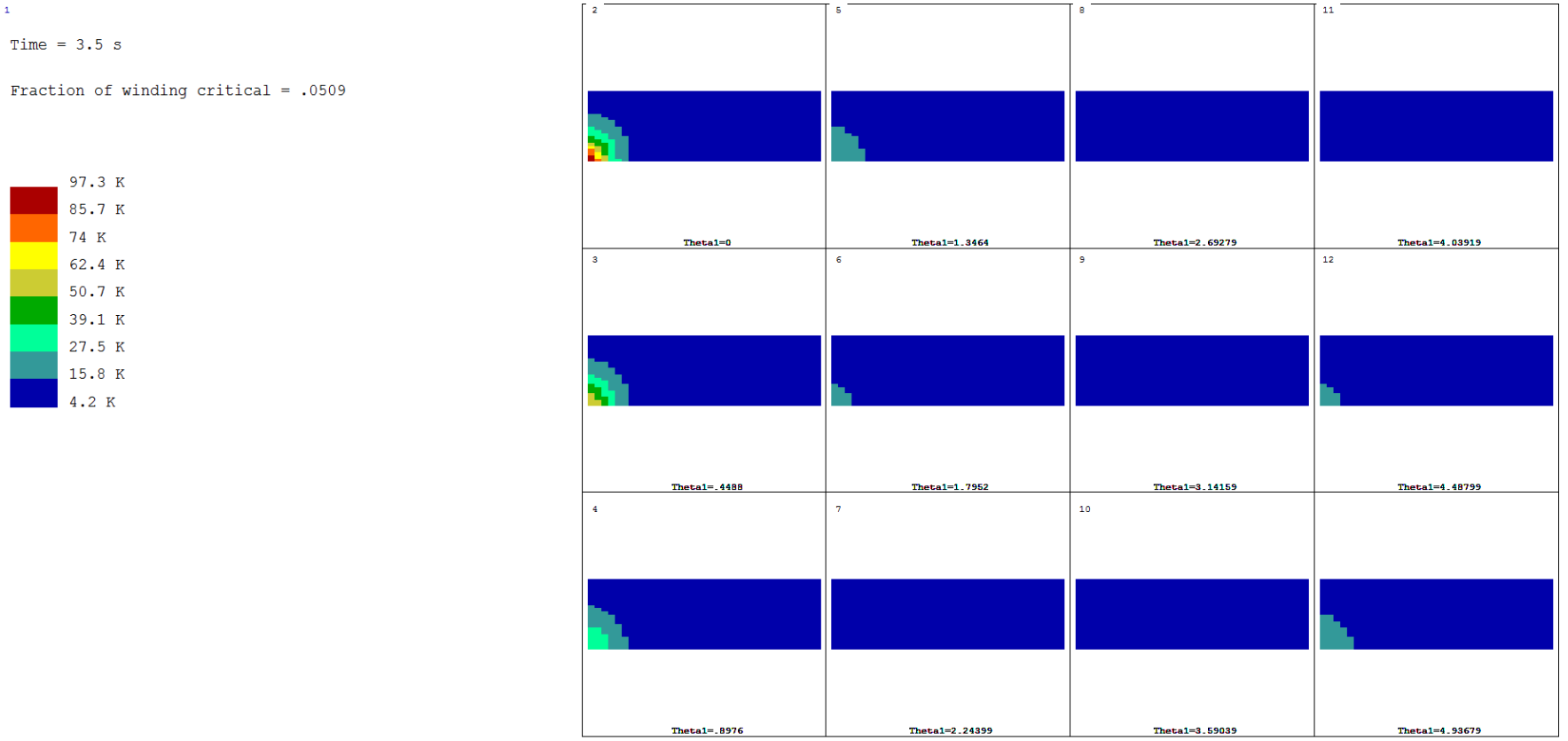

Fig. 7 Temperature distribution at the end of the transient. Hot spot has already cooled from 123 K to 97.3 K. Note that only 5% of the winding is normal and most of the winding is still cold.